Properties of a Mesoscale Convective System in the Context of an Isentropic Analysis

AGNIESZKA A. MROWIEC

Columbia University, and NASA Goddard Institute for Space Studies, New York, New York

O. M. PAULUIS

Courant Institute of Mathematical Sciences, New York University, New York, New York

A. M. FRIDLIND AND A. S. ACKERMAN

NASA Goddard Institute for Space Studies, New York, New York

(Manuscript received 8 May 2014, in final form 7 December 2014)

ABSTRACT

Application of an isentropic analysis of convective motions to a simulated mesoscale convective system is presented. The approach discriminates the vertical mass transport in terms of equivalent potential temperature. The scheme separates rising air at high entropy from subsiding air at low entropy. This also filters out oscillatory motions associated with gravity waves and isolates the overturning motions associated with convection and mesoscale circulation. The mesoscale convective system is additionally partitioned into stratiform and convective regions based on the radar reflectivity field. For each of the subregions, the mass transport derived in terms of height and an isentropic invariant of the flow is analyzed. The difference between the Eulerian mass flux and the isentropic counterpart is a significant and symmetric contribution of the buoyant oscillations to the upward and downward mass fluxes. Filtering out these oscillations results in substantial reduction of the diagnosed downward-to-upward convective mass flux ratio. The analysis is also applied to graupel and snow mixing ratios and number concentrations, illustrating the relationship of the particle formation process to the updrafts.

1. Introduction

Deep convective atmospheric systems, to a first approximation, commonly consist of two regions that differ in terms of size, heating structure, and precipitation intensity. These are the convective cores (the regions of most active convection) and large stratiform regions that produce substantial precipitation but at a rate much less than the cores (Houze 2004). When a mesoscale convective system (MCS) circulation is partitioned into these subregions and upward and downward motions are isolated, small-scale oscillations existing in the studied cloud field get partitioned as well, thus contributing to the mass transport even if mass is not being transported on net. Therefore, we ask the question: is there an effective way to filter out these oscillations when analyzing the properties of the updrafts and downdrafts in the MCS subregions? The theoretical answer is yes, as long as the oscillations are thermodynamically reversible. In this paper, we will show how to apply these principles and the new analytical framework developed in Pauluis and Mrowiec (2013, hereafter PM13) to a cloud-resolving MCS simulation. We also show how to extend this analysis to study microphysical processes within drafts.

Tropical convection is one of the most significant sources of nonorographic gravity waves with a vast spatial and temporal extent (Alexander et al. 1995; Lane et al. 2001). Buoyant air parcels displace ambient air, which adjusts by generating a spectrum of gravitational oscillations (Bretherton and Smolarkiewicz 1989; Mapes 1993). Large-scale atmospheric gravity waves are important for redistribution of momentum and energy, triggering new convection and mixing. They impact the organization of convection on a synoptic scale (Lin et al. 1998) and play an

Corresponding author address: Agnieszka Mrowiec, Columbia University, 2880 Broadway, New York, NY 10025.
E-mail: agni.mrowiec@gmail.com

DOI: 10.1175/JAS-D-14-0139.1

© 2015 American Meteorological Society

important role for coupling of lower- and upper-atmospheric regions (such as the quasi-biennial oscillation, Piani et al. 2000), which is why they are of tremendous interdisciplinary interest (Dunkerton 1997). However, at the opposite end of the gravity wave spectrum are small, virtually omnipresent, buoyant oscillations, which are also generated during the convective events. These oscillations do not contribute to the overall mass transport in the convective overturning but are very difficult to filter out using traditional methods of analysis.

The concept of isentropic analysis can be traced to the early development of meteorology and works by Shaw (1930) and Rossby (1937), who took advantage of the quasi conservation of the potential temperature to track the trajectories of air parcels even when their vertical velocities could not be determined from observations. Averaging air motions on isentropic surfaces—defined either as surfaces of constant potential temperature or equivalent potential temperature θ_e —can also provide insight into the general circulation of the atmosphere. For instance, it is well known that the meridional atmospheric circulation in isentropic coordinates exhibits a single equator-to-pole cell instead of the classic three-cell structure of the Eulerian-mean circulation (e.g., Townsend and Johnson 1985; Pauluis et al. 2008, 2010). The difference between the two representations can be directly linked to the role of the midlatitude eddies in transporting energy and water vapor in the atmosphere (Pauluis et al. 2011).

As recently shown in PM13, this approach can also be applied to a single convective system. In effect, the properties of the flow at each level are conditionally averaged in terms of the air parcels' equivalent potential temperature. Averaging along the adiabatic invariant of the flow sorts the air parcels according to their thermodynamic properties, thus separating the warm moist updrafts from the cooler drier downdrafts. As oscillatory motions associated with gravity waves occur on short time scales, and with little change in θ_e, the isentropic averaging allows for a direct and precise analysis of the convective mass transport while limiting the influence of gravity waves. This method also reduces the size of data that needs to be processed from 4D to 3D, because the isentropic averaging in practice means replacing the two horizontal components (x, y) with one isentropic invariant. It also allows for a better mean representation of the complex 3D parcel trajectories. The isentropic surfaces become the material surfaces, which is especially useful near fronts and in any regions with strong horizontal gradients. It should be noted, however, that the actual parcel trajectories are less likely to conserve the entropy near zones characterized by strong mixing. We discuss some of these caveats later in the paper.

The focus of this paper is twofold. First, we extend the methodology of PM13 to show that it can be successfully applied to capture the evolution of convective activity over a short time scale and within coexisting subdomains. Following Fridlind et al. (2010) and Mrowiec et al. (2012), the cloud-resolving simulation is partitioned into the convective and stratiform regions, within which updrafts and downdrafts are identified. We apply the isentropic analysis of convective motions developed in PM13, expanding the two-stream approximation to multistream, to describe the averaged properties of the subregions (updrafts and downdrafts in the convective and stratiform regions). We also demonstrate how this analysis can be applied to microphysical quantities, such as ice particle number concentrations.

2. Experimental setup

We apply the isentropic analysis to a numerical simulation run in relation to the Tropical Warm Pool International Cloud Experiment (TWP-ICE) centered around Darwin, Australia. A detailed description of the TWP-ICE campaign and synoptic conditions may be found in May et al. (2008). The general goal of the experiment was to understand the relation of convective system properties, including their organization and anvil cloud microphysics, to the properties of the environment on the scale of a GCM grid box so that remote sensing retrievals and multiscale models could be improved. Here, we focus on one particularly strong MCS that formed and moved westward out of the experimental domain on 23–24 January 2006 during the active monsoon period. We present an isentropic analysis of the simulation results; the reader is referred to Varble et al. (2011), Fridlind et al. (2012), Mrowiec et al. (2012), and Varble et al. (2014a,b) for additional plots of precipitation fields and other statistics.

a. Model

The model used in this this study is the Distributed Hydrodynamic Aerosol Radiation Model Application (DHARMA) (Stevens et al. 2002; Ackerman et al. 2000; McFarlane et al. 2002; Ogura and Phillips 1962). The simulation was run on a 176 km × 176 km domain with approximately 900-m horizontal resolution, 96 levels, a stretched vertical grid of 100–250 m, fully periodic lateral boundary conditions, and a model domain height of 24 km. In the simulation, the surface is idealized as oceanic using a fixed ocean surface temperature of 29°C. Each model-calculated grid-scale surface fluxes interactively [see Fridlind et al. (2012) for additional details]. In DHARMA, a second-order forward-in-time dynamics scheme with third-order upwinding advection

(Stevens and Bretherton 1996) is used, as well as a Smagorinsky–Lilly turbulence scheme, a Monin–Obukhov similarity theory for surface fluxes, and two-stream radiative fluxes with ice treated as equivalent spheres (Toon et al. 1989). Simulations are run with a two-moment microphysical scheme described in Morrison et al. (2009), which uses ten prognostic variables: the mass mixing ratios and number concentrations of cloud water, rain, cloud ice, snow, and graupel. The homogeneous freezing (all liquid freezes instantaneously) occurs in the model at −40°C. Between 0° and −40°C, heterogeneous freezing acts to form the ice particles. In DHARMA-2M, the domain is initialized with observation-based trimodal aerosol profiles. As described in Fridlind et al. (2012), aerosol in each mode were advected, consumed by hydrometeor collision–coalescence, and nudged on a domain-mean basis to their initial profiles with a 6-h time scale. Owing to aerosol consumption, which is commonly neglected, the smallest aerosols could consequently be activated in updraft cores (Khain et al. 2012); the realism of such consumption depends on representation of updraft dynamics and microphysics and is the subject of ongoing study. A uniform sea surface temperature of 29°C and surface albedo of 0.07 in all shortwave bands were applied. The large-scale forcings were derived based on variational analysis of observations (Xie et al. 2010) applied at full strength below 15 km and linearly decreasing above to zero strength at 16 km. Mean water vapor and potential temperature was uniformly nudged to mean observed profiles above 15 km with a 6-h time scale. For the analysis presented here, we are using 10-min model outputs. More details of the numerical setup for this simulation are given in previous studies (Fridlind et al. 2010, 2012; Mrowiec et al. 2012; Varble et al. 2011).

b. *Large-scale forcing*

Large-scale forcing data were derived from TWP-ICE radiosonde data using a variational analysis (Zhang 1997) constrained by the surface radiation fluxes, radar-derived precipitation, surface sensible and latent heat fluxes, and the top-of-the-atmosphere radiative fluxes (obtained from surface and satellite observations). The variational analysis requires initial temperature, wind, and humidity fields, which were generated using the European Centre for Medium-Range Forecasts (ECMWF) analysis [see Xie et al. (2010) for more details]. As a result, large-scale vertical velocity and advective tendencies for potential temperature and water vapor fields were created. The potential temperature and water vapor fields in the simulations were forced by these advective tendencies below 15 km, and the condensate was forced by the vertical tendency calculated using the large-scale vertical velocity. The impacts of this large-scale forcing on the following analysis will be discussed in section 5.

c. *Convective–stratiform partitioning*

The cloud field simulated in this study was divided into convective and stratiform rain regions using a horizontal textural algorithm, which identifies regions of active convection (Steiner et al. 1995), as in Mrowiec et al. (2012). The Steiner algorithm consists of three steps applied to the gridded radar reflectivity field at a chosen elevation below the melting level. Therefore, both convective and stratiform regions are, by design, associated with precipitation. Icy anvil clouds that do not have precipitation reaching low levels are not included in the stratiform-region definition in this classification.

To apply the partitioning to model output, Rayleigh radar reflectivity was calculated at 2.5-km altitude for each simulation (for reference, we add that the melting level is at about 5 km). The first step of the partitioning process is to identify the convective cores and include their surrounding area based on reflectivity values of peakedness. This is done to assure that the neighboring convective cores that are close enough belong to the same convective patch. The remainder of the precipitating grid points (selected using a minimum threshold of 0 dBZ) is then assumed to be part of the stratiform region [see Fridlind et al. (2012) for details of the method as applied in this case]. Each time step includes different stages of convective development and the boundary between convective and stratiform regions is not always sharp. Often there is a region with mixed properties in between. Thus, identified stratiform regions may include some shallow convection or some transition structures. Several studies (e.g., Biggerstaff and Houze 1991, 1993; Del Genio and Wu 2010) took this into account by defining a separate transition region. For our objectives, this added complexity is unnecessary, and we limit ourselves to ensuring that our stratiform regions are deep by imposing a requirement of the minimum reflectivity of 5 dBZ at 6-km altitude within them. A remaining area, which one could be inclined to call a "clear sky," does not have to be cloud free. It includes clear-sky, nonprecipitating clouds, and anvil clouds with precipitation that does not reach the low levels. That is because the radar typically does not see the small cloud or ice particles; therefore, the algorithm used for partitioning was designed to extract only the precipitating regions. This method is widely used in particular because it allows for direct comparison between models and observations (Lang et al. 2003), and it is also perfect for Darwin because it was developed using radar data specifically from this location. After applying the partitioning algorithm,

we define three masks—$H_C(x, y, t)$, $H_S(x, y, t)$, and $H_{NP}(x, y, t)$—that are respectively equal to 1 in the convective, stratiform, and nonprecipitating portions of the domain and 0 elsewhere.

3. Isentropic averaging

In this study, we use the isentropic technique developed in PM13 and transform the Cartesian horizontal coordinates (x, y) into an isentropic coordinate. This contrasts with the traditional use of the isentropic analysis in synoptic meteorology, in which the vertical coordinate z is replaced by a thermodynamic coordinate. Here, air parcels with similar thermodynamic properties can be followed (in an averaged sense), as they are carried by convective updrafts and downdrafts, and a mean isentropic overturning circulation can be determined.

a. Identifying the convective, stratiform, and nonprecipitating mass flux

There is a certain freedom in the choice of the thermodynamic variables used for identification of isentropic surfaces. Because of deep convection, the average temperature profile in the tropics is close to the moist adiabat (Xu and Emanuel 1989), which makes θ_e a good candidate for an invariant of the flow. Here, we base the isentropic calculations on θ_e, defined as

$$\theta_e = \frac{T}{\Pi}\mathcal{H}^{-R_v q_v/C}\exp\left(\frac{L_v q_v}{CT}\right),$$

where T is temperature, $\Pi = (p/p_0)^{R_d/C}$ is the Exner pressure, p_0 is reference pressure, R_v and R_d are the gas constant of water vapor and dry air, respectively, C is given by $C = c_p + c_l q_t$ following Emanuel (1994, his Eq. 4.5.11), with c_p and c_l being the specific heat at constant pressure of dry air and liquid water, q_t is a total water mixing ratio, L_v is the latent heat of vaporization, $\mathcal{H}$ is the relative humidity, and q_v is the water vapor mixing ratio. Condensation and precipitation have little impact on θ_e; thus, the change in it in the free troposphere is mainly caused by entrainment, radiative cooling, and ice fallout (Emanuel 1994). Precipitation of water has a very small impact on θ_e, because the specific entropy of liquid water is small, but freezing and ice fallout do increase θ_e. Averaging in isentropic coordinates captures the mean convective transport of air from surface (where latent and sensible heat fluxes are the sources of θ_e) to the cloud top (where radiative cooling is a sink of θ_e).

Following PM13, the isentropic mass flux is defined as a horizontal mean over all parcels with a specified value of θ_e:

$$\langle M\rangle(\theta_e, z, t) = \frac{1}{L^2}\iint \overline{\rho_o}(z)[w(x,y,z,t) - \overline{w}(z,t)]\delta(\theta_e - \theta_e')\,dx\,dy, \tag{1}$$

where $\overline{\rho_o}(z)$ is the mean atmospheric density profile, $w(x, y, z, t)$ is the vertical wind component, $\overline{w}(z, t)$ is the horizontal mean of the resolved vertical wind (which is zero for this simulation setup, as required by the doubly periodic boundary conditions, but does not have to be in general), and L is the horizontal length of a square domain. In practice, the Dirac function $\delta(\theta_e - \theta_e')$ is approximated by a piecewise constant function equal to $\Delta\theta_e^{-1}$ for $-\Delta\theta_e/2 < \theta_e - \theta_e' < \Delta\theta_e/2$ and 0 elsewhere, so that $\langle M\rangle$ is computed by adding the vertical mass flux over finite θ_e bins at each vertical level and each time step. The contributions of the convective (C), stratiform (S), and nonprecipitating (NP) regions to the isentropic mass flux can be similarly defined as follows:

$$\langle M\rangle_C(\theta_e, z, t) = \frac{1}{L^2}\iint \overline{\rho_o}(z)[w(x,y,z,t) - \overline{w}(z,t)]\delta(\theta_e - \theta_e')H_C\,dx\,dy; \tag{2a}$$

$$\langle M\rangle_S(\theta_e, z, t) = \frac{1}{L^2}\iint \overline{\rho_o}(z)[w(x,y,z,t) - \overline{w}(z,t)]\delta(\theta_e - \theta_e')H_S\,dx\,dy; \quad \text{and} \tag{2b}$$

$$\langle M\rangle_{NP}(\theta_e, z, t) = \frac{1}{L^2}\iint \overline{\rho_o}(z)[w(x,y,z,t) - \overline{w}(z,t)]\delta(\theta_e - \theta_e')H_{NP}\,dx\,dy. \tag{2c}$$

The isentropic mass fluxes averaged over the duration of the convective event are shown in Fig. 1 in terms of equivalent potential temperature and height for the domain as a whole and in the convective, stratiform, and nonprecipitating regions. The following figures show the results at and above 500 m. The surface layer, where θ_e hugely increases, is not relevant to the present study. Showing it would change the horizontal scale of the

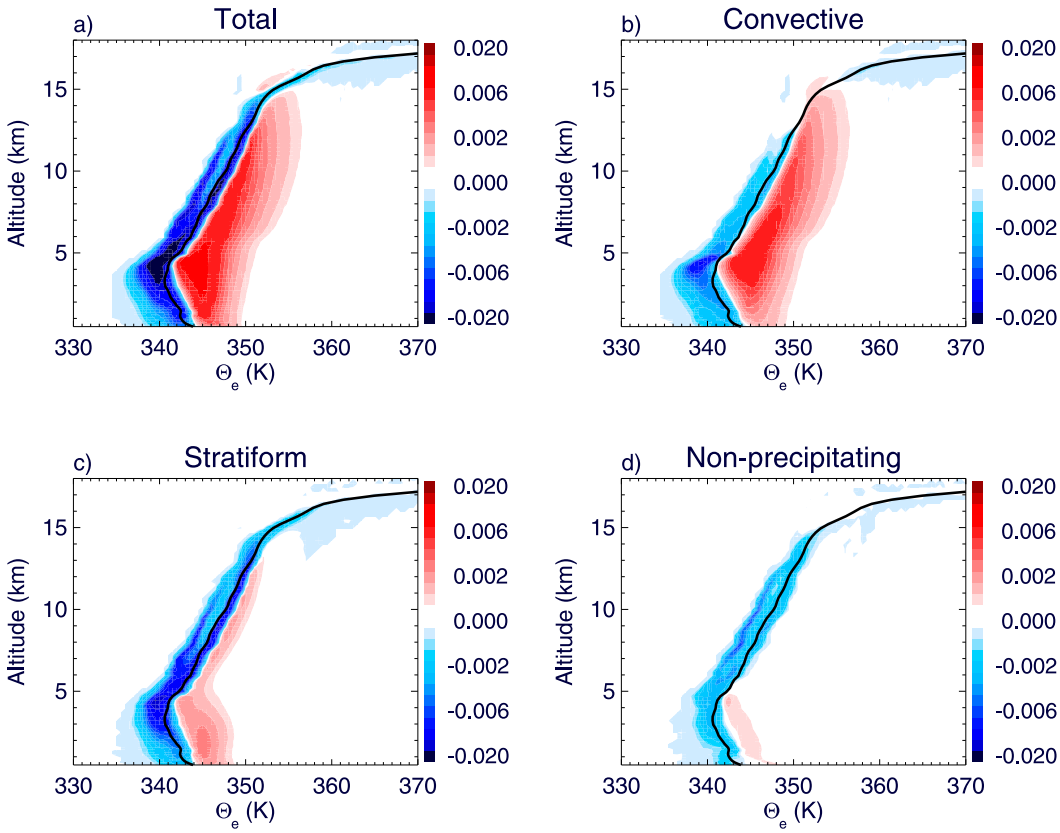

FIG. 1. Time-averaged isentropic mass flux (kg m^{-2} s^{-1} K^{-1}) for (a) the whole domain and in the (b) convective, (c) stratiform, and (d) nonprecipitating regions. The black solid line marks the mean environmental equivalent potential temperature profile. The convective region mass flux maximum is around the melting level. In the stratiform region, there is a low-level overturning circulation in addition to the downdrafts. Stratiform ascent is weak. In the nonprecipitating region, there is a large-scale descent present.

figures and distract from the actual results. The mass transport for the whole domain exhibits a typical structure associated with convective overturning. The air is rising at θ_e warmer than the domain mean and subsiding at θ_e lower than the domain mean, which is a structure directly tied to a net upward transport of energy and equivalent potential temperature. The maxima of upward and downward mass fluxes are centered around 5 km. This result is in contrast to the isentropic mass transport in the radiative–convective equilibrium (RCE) simulations of PM13 (their Fig. 1a), which have the bulk of the overturning circulation located below 5 km. For reference, the RCE simulation was performed with the System for Atmospheric Modeling (SAM; Khairoutdinov and Randall 2003) integrated over 100 days on a 216 km × 216 km horizontal domain at 500-m resolution and 28 km stretched over 64 vertical grid points. The horizontal boundaries were periodic, and the surface had a constant temperature of 301 K. A sponge layer was applied in the top 8 km of the domain. In the RCE case, the convection is initiated at the surface and is mostly relatively shallow. The upward mass transport happens at the equivalent potential temperature values that are much higher than the mean θ_e profile. However, the downward mass flux in the RCE simulations happens at the equivalent potential temperatures surrounding the mean profile values, which corresponds to the large-scale imposed subsidence in the simulation. This is different from the present MCS case in which, above the melting level ($z \approx 5$ km), the descending air peaks at two equivalent potential temperature values: one close to the horizontal mean $\overline{\theta_e}(z)$ associated with the slow subsidence of air through the domain, and the other colder, associated with the nonconvective downward motions at the beginning of the simulation. Below the melting level, there is a notable amount of descending air for θ_e much lower than the domain average. This is a signature of downdrafts, which can be seen in both the convective and stratiform regions (Figs. 1b,c).

When the domain total isentropic mass flux (Fig. 1a), introduced in Eq. (1) and time averaged, is partitioned between the convective and stratiform regions [Figs. 1b

and 1c, expressed by time-averaged Eqs. (2a) and (2b), respectively], it can be seen that the bulk of the ascending motion happens within the convective towers but does not peak near the surface but instead closer to the melting level. This feature of the upward mass flux, differs from the RCE simulations and is correlated with the increase of the equivalent potential temperature with height. For an adiabatic ascent, θ_e would be conserved. In reality, θ_e is expected to decrease as a result of entrainment of drier and cooler environmental air into the convective plumes; indeed, PM13 showed that the θ_e in the ascending branch of the isentropic circulation decreased with height in their simulations. There are two potential causes to this increase in equivalent potential temperature: first, freezing increases θ_e even for adiabatic ascent, and second, the strong large-scale forcing (Mrowiec et al. 2012; Xie et al. 2010), which increases θ_e during the active monsoon phase through the convergence of water vapor and heat. We will revisit the issue of the downward mass transport in more detail when addressing the large-scale forcing in section 5.

In the stratiform region, weak ascent is present above the melting level. There is an overturning associated with shallow convection, but it does not cross the melting level ($z \sim 5$ km). There is no significant ascent in the nonprecipitating region. Considerable downward mass transport occurs in all regions as low-entropy air is forced downward to compensate for the rising air in the updrafts. In downdrafts, θ_e decreases moving from the tropopause toward the melting level and then increases moving from the melting level toward the surface as a result of precipitation reevaporation. In the stratiform and nonprecipitating regions, the downward mass fluxes show a double maximum above the melting level. This feature may be explained by the initial subsidence during which the temperatures are cool, then a strong burst of convection that mixes up and warms the troposphere, resulting in descending motions that are warmer and closer to the domain mean. The melting level is situated slightly below 5 km and has several effects on the isentropic mass transport. As noted earlier, the upward mass flux in both the stratiform and clear-sky regions decreases strongly at the melting level, indicating that stratification acts as a barrier to weak convective updrafts. Finally, a large downward mass flux appears for $335 < \theta_e < 340$ K at the melting point. This air has an equivalent potential temperature that is considerably lower than the mean value at any point in the domain. Such low equivalent potential temperature can be explained by the melting of frozen precipitation, which reduces θ_e in the surrounding air. The isentropic analysis further indicates that this air moves down toward the surface in convective and stratiform regions, thus confirming the role played by convective and mesoscale downdrafts in the simulation.

Convective overshoot can be detected through the combination of the isentropic analysis and convective–stratiform partitioning. The convective regions exhibit a net ascent near the tropopause for $z = 15$ km and $\theta_e = 352$ K (Fig. 1b). The stratiform regions show a net downward motion (Fig. 1c). This is directly tied to air parcels piercing the tropopause as they rapidly rise within convective towers and then slowly settling back to their level of neutral buoyancy within the stratiform area. As the subsidence in the stratiform regions balances out the ascent in the convective regions, this overshoot is partially masked in the total isentropic mass transport.

b. Comparison with Eulerian analysis

The upward and downward mass fluxes can be computed without the isentropic averaging, but this can result in including oscillatory motions, such as gravity waves in the directional mass flux. To see what portion of the mass flux can be attributed to the oscillations, it is best to compare the mass fluxes defined in both Eulerian and isentropic frameworks. The upward and downward Eulerian mass fluxes within the convective region are respectively defined as follows:

$$M_C^+(z,t) = \frac{1}{L^2}\iint \rho_0(w-\overline{w})H_C H(w-\overline{w})\,dx\,dy \quad \text{and} \tag{3a}$$

$$M_C^-(z,t) = \frac{1}{L^2}\iint \rho_0(w-\overline{w})H_C H(\overline{w}-w)\,dx\,dy. \tag{3b}$$

Here, the updrafts and downdrafts are partitioned using a Heaviside step function, which takes into account the positive and negative vertical velocity. Unlike in the isentropic formulation, there is no averaging over θ_e bins. In this example, the mass fluxes are shown for convective region; thus, the mask used is H_C. These definitions can be applied to specify the upward and downward Eulerian mass flux in the stratiform and clear-sky regions as well, using appropriate step-function conditions.

Similarly, the upward and downward isentropic mass fluxes are defined as follows:

$$\langle M\rangle_C^+(z,t) = \int \langle M\rangle_C H(\langle M\rangle_C)d\theta_e' \quad \text{and} \tag{4a}$$

$$\langle M\rangle_C^-(z,t) = \int \langle M\rangle_C H(-\langle M\rangle_C)d\theta_e', \tag{4b}$$

which can be defined in the stratiform and clear-sky regions as well. The isentropic upward mass flux is summed over all equivalent potential temperature points that have

a positive, convective mass flux $H(\langle M\rangle_C)$. Similarly, a definition is applied to the downward mass flux, but using only the points in θ_e–z space with negative mass flux values.

In Fig. 2, the upward and downward mass fluxes in convective, stratiform, and nonprecipitating regions are shown for the isentropic and the Eulerian mass flux components. These fluxes are averaged over the duration of the convective event and normalized by the horizontal area. On average (time and space), the convective regions occupy 12.7% of the domain area, the stratiform regions occupy 57.1%, and nonprecipitating regions occupy 30.2%. Despite the relatively small area, the convective regions account for the bulk of the ascent. The stratiform regions are associated with strong subsidence, and the nonprecipitating region is comparatively quiescent, with only weak subsidence. This result is consistent with intense ascending motion in the deep convective towers, combined with reevaporation-driven descent in the stratiform regions. We note that stratiform regions are commonly associated with ascent above the melting level rather than descent, as discussed further in section 5. The difference between the Eulerian and isentropic mass fluxes shows a notable, symmetric contribution (of equal magnitude) of the buoyant oscillations to the mass flux signal in the updrafts and downdrafts in the subregions of a convective system. This symmetry arises directly from the fact that the net mass flux should be equal; that is,

$$M_i^+ + M_i^- = \langle M\rangle_i^+ + \langle M\rangle_i^-$$

for each of the individual subregions (i = C, S, or NP). The core difference between the Eulerian [Eqs. (3a) and (3b)] and isentropic [Eqs. (4a) and (4b)] definitions is that the separation between ascending and descending motions is done after the flow has been averaged on isentropic surfaces rather than on the instantaneous direction of the flow. This means that fast adiabatic oscillations are averaged out, but upward transport associated with mixing and irreversible overturning is not. Because of this partial cancellation, the isentropic directional flow is always less than the Eulerian equivalent, and the difference between the two can be thought of as a measure of reversible oscillatory motions in various convective subregions.

In the convective regions, the isentropic analysis shows strong ascent through the entire troposphere but only limited descending motion concentrated below the melting level. By contrast, the Eulerian diagnostic indicates more pronounced descending motion above the melting level. In this regard, the Eulerian mass transport tends to include a large contribution from buoyant oscillations to the upward and downward mass fluxes. In

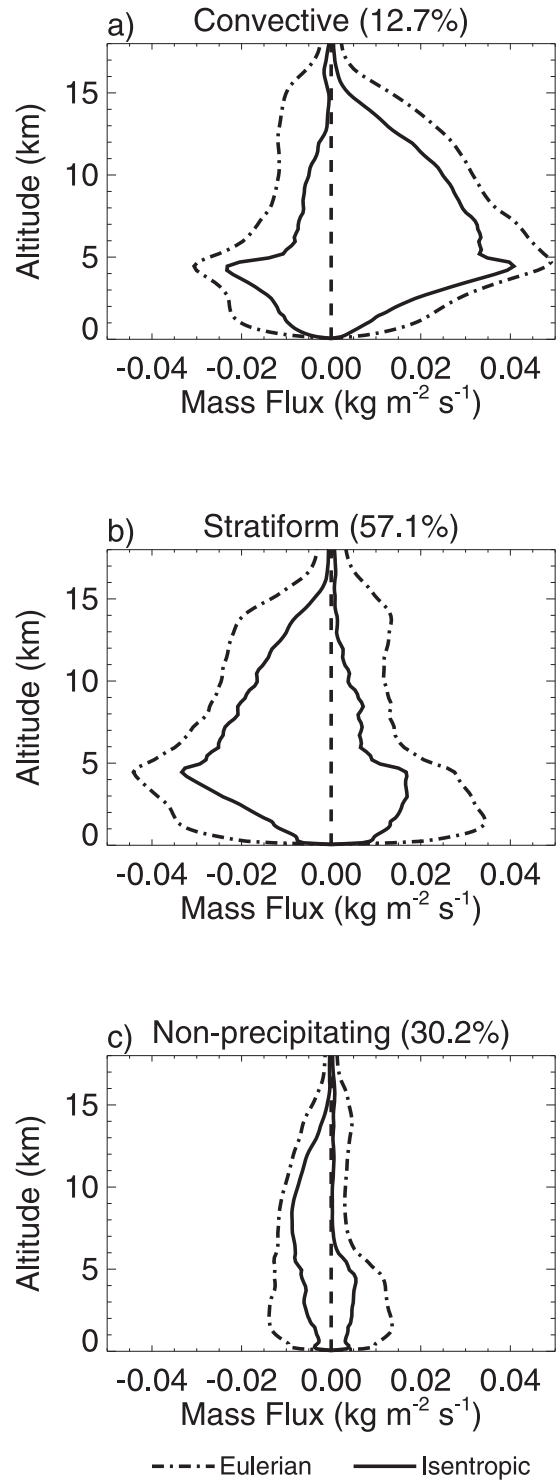

FIG. 2. Eulerian (dotted–dashed) and isentropic (solid) upward and downward mass fluxes ($\mathrm{kg\,m^{-2}\,s^{-1}}$) in (a) convective, (b) stratiform, and (c) nonprecipitating regions. The fields were averaged over the duration of the convective event. The difference between dashed and solid lines is symmetric between upward and downward mass transport, and it shows the averaged contribution from the reversible oscillations.

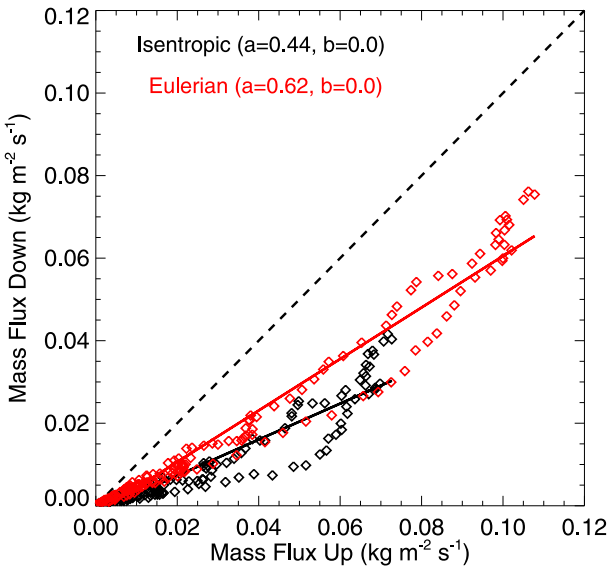

FIG. 3. Convective-region updraft vs downdraft mass fluxes at each model time step for isentropic (black) and Eulerian (red) mass fluxes. Points were fitted with the linear functions shown with solid lines.

particular, the descending motion above the melting level diagnosed with M_C^- indicates the presence of gravity waves but has little relationship to convective downdrafts.

In the stratiform regions, the picture is reversed: there is a strong downward flux through the depth of the domain, while the isentropic ascent is mostly confined to the lower troposphere. The Eulerian analysis strongly overestimates the upward mass flux in the stratiform anvil clouds by including a large contribution from the oscillations. In the nonprecipitating region, there is no isentropic ascent above the melting level. The ascending motion diagnosed by the Eulerian mass flux M^+ is an artifact of the averaging procedure (the gravity wave regions contribute approximately equally to positive and negative deviations beyond the isentropic analysis estimate), which includes a net contribution for oscillatory motions from gravity waves.

This fact has implications for the downward-to-upward mass flux ratio as well. As pointed out in Mrowiec et al. (2012), the mass flux closure–based convection parameterizations typically assume that the downward mass flux is a constant fraction of the upward mass flux. The isentropic and Eulerian downward versus upward mass flux in the convective regions are shown in Fig. 3. Points are shown at each model time step and were fitted with a linear function to obtain the ratio in question. The removal of the buoyant oscillations, which symmetrically reduces both mass fluxes, results in a lower value (0.44) of the downward-to-upward mass flux ratio. We note that the points follow a loop rather than a line, with the lower branch marking the buildup stage of the convective event and the upper branch referring to the decay stage.

c. *Isentropic streamfunction, vertical velocity, and buoyancy*

Once the mass flux is defined, the isentropic streamfunction may also be calculated as an integral of the mass flux over a potential temperature range:

$$\overline{\Psi}(\theta_e, z) = \int_{\theta_{e,\min}}^{\theta_e} M(\theta_e', z)\, d\theta_e'. \tag{5}$$

A streamfunction defined this way illustrates the vertical overturning circulation carried out by the convective system and corresponds to the upward entropy transport, which makes it negative throughout the depth of the troposphere. The isentropic streamfunction is shown in Fig. 4a. The domain-mean θ_e profile is shown by the solid white line. The absolute minimum of the streamfunction is located at the melting level. As was demonstrated in PM13 (their Fig. 1b), for the radiative–convective equilibrium the strongest values of the streamfunction were located near the surface, because that is where the forcing for the convection is located. Here, the large-scale forcing driving the simulation was quite strong and not peaked at the lowest levels shown. For the sake of curiosity, we looked at the isentropic streamfunction in one of the limited-area model (LAM) simulations of this MCS case, described in Zhu et al. (2012) (not shown). As reported by Zhu et al. (2012), although LAM simulations differ from one another and from the observations in their simulated cyclogenesis, there is a general consistency between cloud-resolving model (CRM) and LAM simulation stratiform and convective dynamics and cloud properties, including a large spread across microphysics scheme results within each model class. The result was similar to the present simulation. At this point, we cannot definitely state if the elevated convective overturning maximum (which is representative of this simulation) is a property of the strong convective systems or if, to some extent, it is related to the TWP-ICE case study setup. It is an interesting question that warrants further investigation in the future.

The magnitude of the streamfunction decreases above 5 km. Ascending air parcels originating from the lowest atmospheric layer start with high values of θ_e of about 345 K. The equivalent potential temperature does not drop rapidly with height for the isocontours of the streamfunction, as expected in the case of strong entrainment of drier air in the updrafts. Instead, there is generally a slight increase throughout the troposphere. We suspect that the strong forcing in this case is aided by

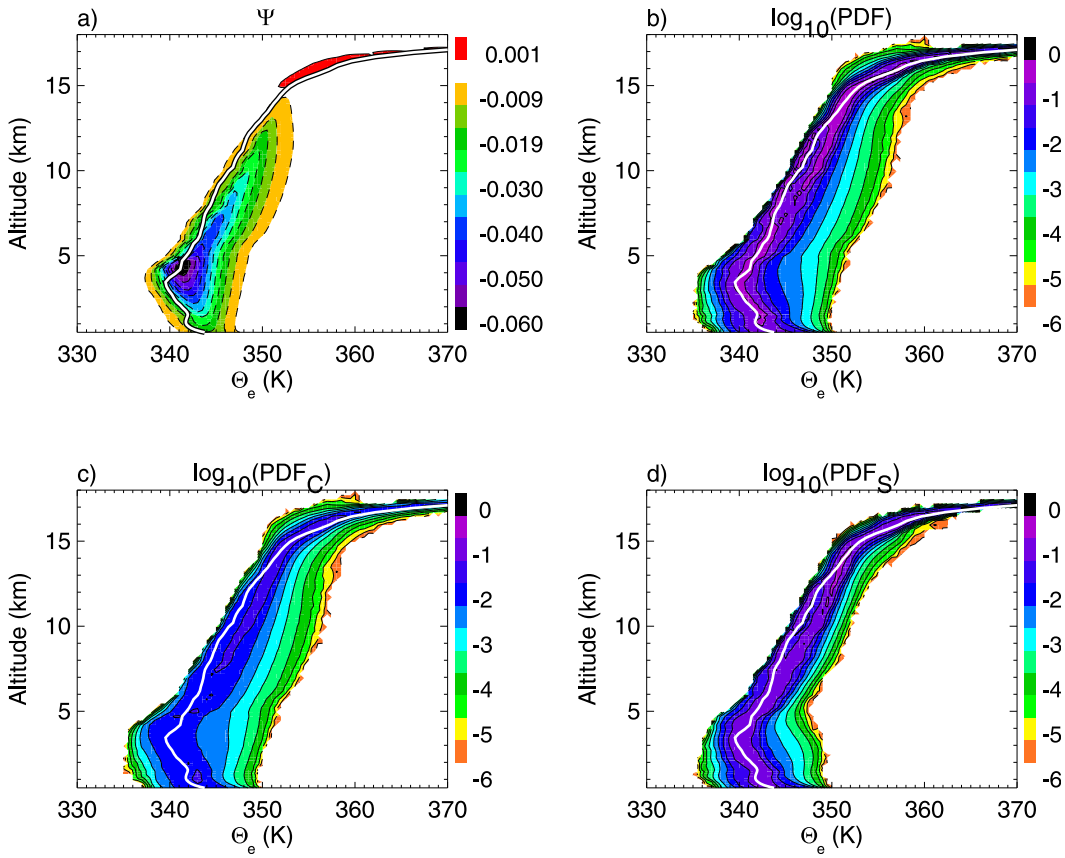

FIG. 4. (a) Time-averaged isentropic streamfunction for the whole domain. The overturning circulation maximum (or the absolute minimum of the streamfunction) is located at the melting level, which implies a strong large-scale forcing of the simulation. White solid lines mark the mean environmental equivalent potential temperature profile. Frequency of occurrence of parcels at a given height and θ_e for the (b) whole domain, (c) convective regions, and (d) stratiform regions.

a contribution from freezing producing the θ_e increase. The sign of the streamfunction changes to positive at about 15 km, which may be attributed to the presence of a convective overshoot and a downward entropy transport.

Figure 4b illustrates the frequency of occurrence of air parcels with a specific value of equivalent potential temperature for the whole domain, and Figs. 4c and 4d illustrate the frequency of occurrence partitioned between convective and stratiform regions. The warmest updrafts (in terms of θ_e) are the least frequent, and they are located only in the convective regions. The coldest downdrafts occur at low levels, and they are much less frequent than extreme drafts on the updraft side of the motions. The majority of air parcels are grouped around the mean domain profile. In the stratiform region, the air parcels stay closer to the domain mean than in the convective region. The distribution of the parcel concentration is not symmetric around the mean; in particular, for the convective region it skews toward high values of θ_e.

The isentropic averaging in combination with the isentropic density can also be used to define the isentropic-mean distributions of a number of parameters:

$$\tilde{f}(z,\theta_e) = \frac{\langle \rho f \rangle (z,\theta_e)}{\langle \rho \rangle (z,\theta_e)}, \tag{6}$$

where f may be any variable (such as vertical velocity, buoyancy, or the microphysical property) and $\tilde{f}$ is an isentropic mean of that variable. The isentropic mean is defined in the mass-weighted sense. In some situations, there is no difference between the mass-weighted average and the regular average (e.g., when using anelastic model solutions). For the anelastic model, air density $\overline{\rho}z$ depends only on height, and Eq. (6) can be reduced to form

$$\tilde{f}(z,\theta_e) = \frac{\langle f \rangle (z,\theta_e)}{\langle 1 \rangle (z,\theta_e)}, \tag{7}$$

where $\langle 1 \rangle$ is the probability density function defined in PM13 [Eq. (4)] and has units of per kelvin. The

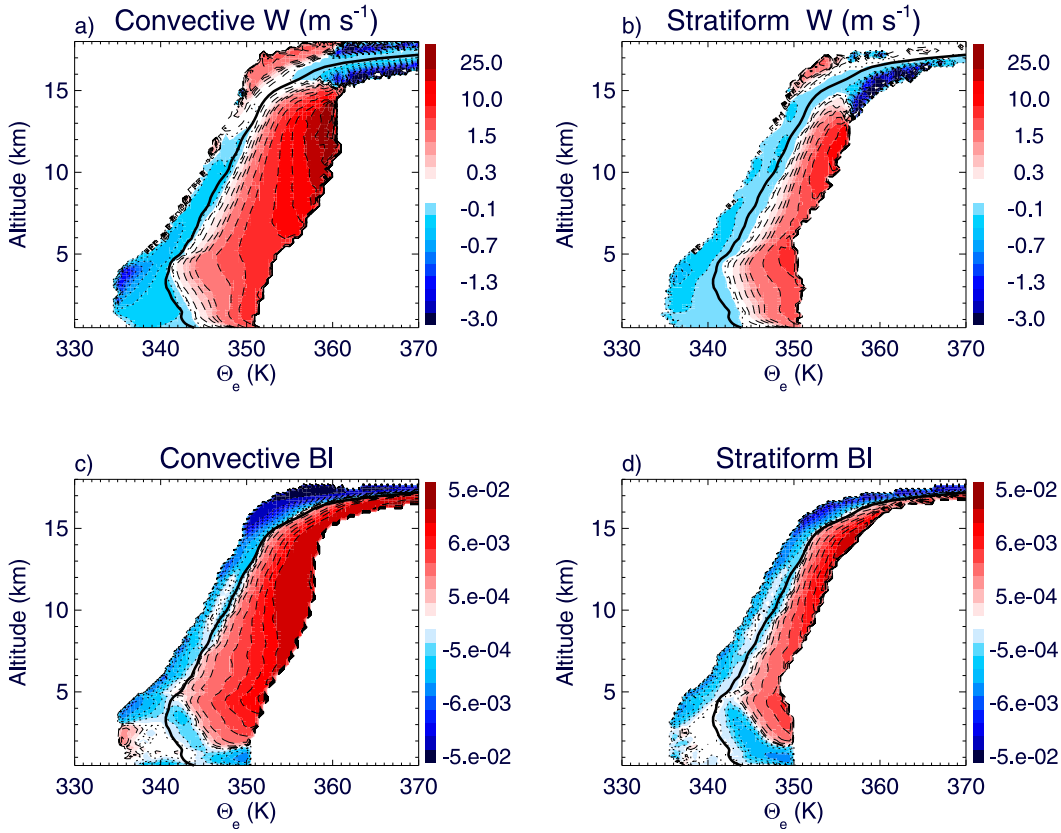

FIG. 5. (top) Isentropic vertical air velocity in (a) convective and (b) stratiform regions, and (bottom) buoyancy in (c) convective and (d) stratiform region. The black solid line marks the mean environmental equivalent potential temperature profile.

atmosphere is not anelastic. For compressible fluids with high-density fluctuations or turbulence, a mass-weighted averaging is the preferred approach. Additionally, the isentropic averaging changes the dimensionality of averaged parameters. The isentropically averaged density $\langle\rho\rangle$, is not the same as, for example, spatially averaged density. In the process of isentropic averaging, the density is multiplied by the probability density function [PM13, Eq. (4)] shown in Fig. 4b; as a result, $\langle\rho\rangle$ has units of kilograms per cubic meter per kelvin. The formulation of isentropic-mean distribution defined in Eq. (6) allows it to return to the standard parameter dimensions.

Increase with altitude in updraft equivalent potential temperature can also be observed in the isentropic representation of the time-mean vertical velocity, which is shown in Fig. 5a for convective and Fig. 5b for stratiform regions. Strong convective updrafts accelerate through the melting level with height to reach a maximum at about 12–13 km. The fastest convective updrafts observed in the upper troposphere may correspond to infrequent undiluted or weakly diluted air parcels. The stratiform updrafts show a maximum in the boundary layer and a stronger maximum at about 12 km. The boundary layer maximum is most likely a signal of shallow convection, which is often collocated with the stratiform region. Weak stratiform ascent (compared to downdraft) extends from about 9 to 14 km. Most ascent in a stratiform region is on the order of centimeters per second (see Fig. 5b combined with Fig. 4d). Note that the strongest updrafts are much stronger than the strongest downdrafts, consistent with the RCE results (PM13). Downdrafts reach the minimum equivalent potential temperature of about 335 K at the melting level. Some downdrafts get warmer as they approach the lower levels because of the mixing with detrained warmer cloudy air or with the environment, which has a higher θ_e.

Figures 5c and 5d show time-averaged buoyancy with water loading, defined as $B_{\mathrm{wl}} = (\theta_v - \overline{\theta_v})/\overline{\theta_v} - q_h$, where θ_v is the virtual potential temperature and q_h is the water loading, in the convective and stratiform regions, respectively. The lowest buoyancy at the melting level is tied to the melting of precipitation in unsaturated air. This is the location of the strongest downdrafts in both convective and stratiform regions. Upper-level buoyancy and vertical velocity for a given value of θ_e are fairly uniform with height in the convective regions, especially

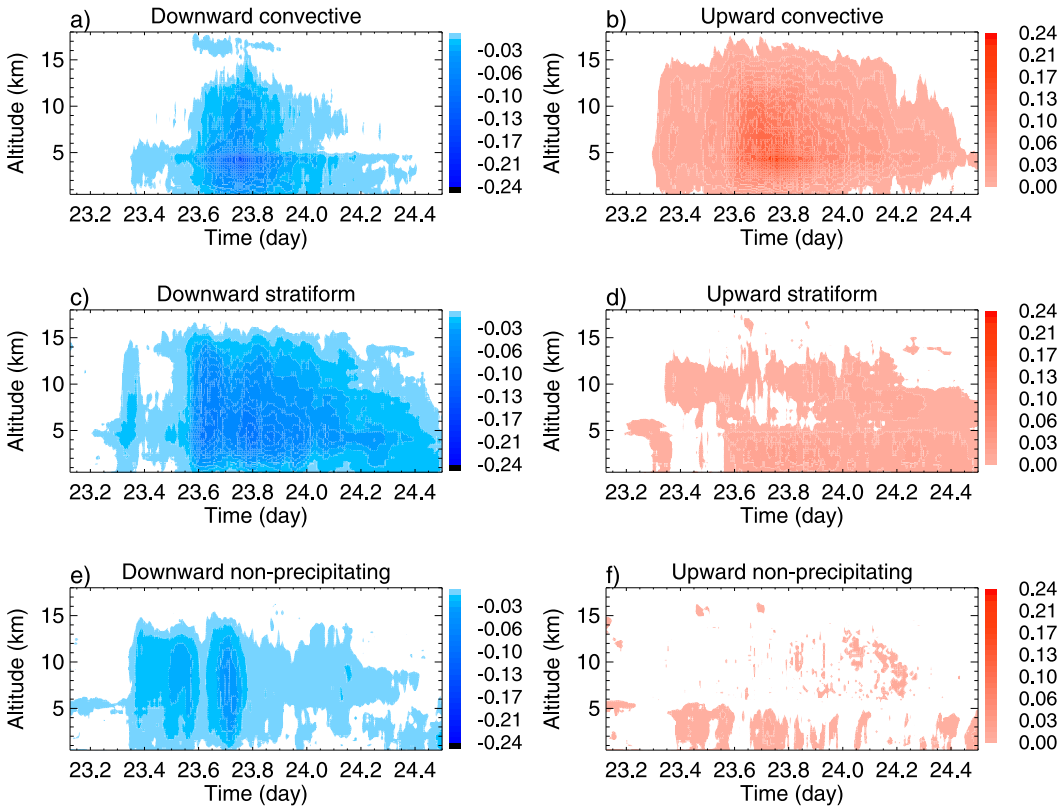

FIG. 6. Time series of (a),(c),(e) downward and (b),(d),(f) upward isentropic mass fluxes (kg m^{-2} s^{-1}) in the convective, stratiform, and nonprecipitating regions. The majority of the upward mass transport is concentrated in the convective towers; however, the downward mass transport is distributed between the convective and stratiform regions.

at higher values of θ_e. Precipitation affects buoyancy through the drag of condensed water, evaporation, and melting (Emanuel 1994). Condensate and precipitation particles exert drag forces on the parcel of air equal to the weight of the condensate. Roughly 3 g kg^{-1} of condensate is equivalent to 1 K of negative thermal buoyancy. Typically, evaporation dominates over the impacts of melting because the latent heat of vaporization is 8 times larger than that of freezing. Below the melting level, however, the melting process can have a very strong, local impact on enforcing negative buoyancy [also noted in Grim et al. (2009)].

4. Evolution of the isentropic mass flux

To illustrate the evolution of convection within this simulation, the profile time series of total upward and total downward isentropic mass fluxes for the convective system's subregions are plotted in Fig. 6. Deep upward mass transport is mostly located in convective towers, with the maximum around the melting level. There is not much contribution from the stratiform region (very weak stratiform ascent) and even less from the rest of the domain. An initial, weaker burst of convection occurs at 0700 UTC 23 January (day 23.3), with a few isolated convective towers. The main convective activity starts at 1200 UTC (day 23.5, almost 5 h later), as shown in the convective upward mass transport (Fig. 6a). The upward motions are correlated with convective and stratiform downdrafts, the former peaking at the melting level, and the latter being more evenly distributed throughout the troposphere. In the stratiform region, following the onset of deep convection, there is a low-level overturning that may be seen below the melting level. There is no significant upward mass transport in the nonprecipitating region, but there is some subsidence. Past the peak of the convective event, almost the entire domain is occupied by either convective or stratiform clouds; therefore, the contribution to the downward mass transport by the nonprecipitating region almost completely disappears.

As was mentioned earlier, one of the advantages in using isentropic averaging is that the buoyant oscillations are naturally removed from the analysis of the convective subregions. The evolution of the difference between the Eulerian and isentropic downward mass

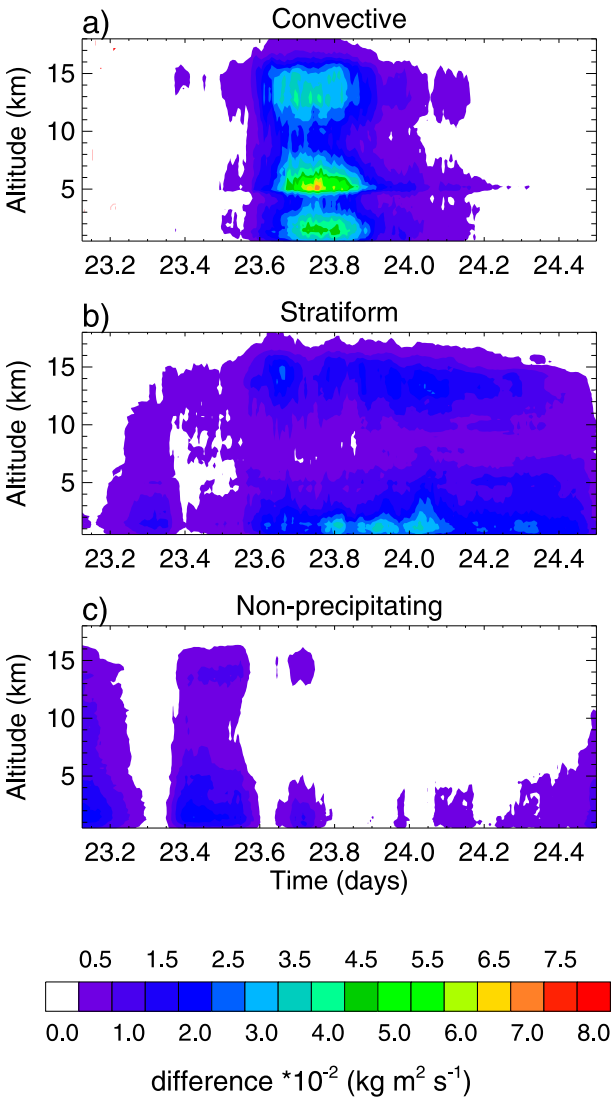

FIG. 7. Time series of the difference between the Eulerian and isentropic downward mass flux in the (a)convective, (b) stratiform, and (c) nonprecipitating regions.

fluxes for the convective, stratiform, and nonprecipitating regions is shown in Fig. 7. The difference itself is symmetric; therefore, we show only the downward mass flux difference. This discrepancy demonstrates the timing and location of the oscillations. The oscillations are temporally correlated with the convective activity. The main burst of convection induces buoyant oscillations in the convective region. The main sources of the gravity waves are in the boundary layer (as a result of boundary layer turbulence), at the tropopause (where convection overshoots the level of neutral buoyancy and radiates gravity waves), and in the midlevels. The midlevel oscillation source is located at the melting level and only in the convective region. We speculate that this source is caused by graupel formation just above the melting level, which gives the updrafts a buoyancy boost and induces oscillations with a small horizontal extent and strong vertical group velocity [as also shown in Varble et al. (2014a,b)]. In the stratiform region, there are only the boundary layer–related oscillations and the tropopause oscillations that propagated away from the convective towers. The timing in the stratiform and nonprecipitating regions is not as clear-cut as in the convective region. In these two regions, some residual oscillations are present almost from the start of the analysis period.

5. Large-scale forcing impacts

The active monsoon period is characterized by strong upward motions and large advective cooling and moistening through the depth of the troposphere. Figure 8a shows the large-scale vertical velocity field that is the basis of the horizontally uniform vertical forcing used in the simulation. Large-scale forcing is derived from variational analysis of observed sounding-array profiles and surface rain-rate retrievals, among other observational inputs [see Xie et al. (2010) for additional details]. Although the absolute values of the large-scale vertical wind may appear weak in comparison with the strong convective updrafts, they are enough to neutralize the downdrafts in the stratiform and nonprecipitating regions. The large-scale forcing was likely moistening the lower troposphere (Fridlind et al. 2010) and enhancing θ_e in the updrafts. The rainfall rate at the surface is shown in Fig. 8b for the simulation and the observations from the C-band polarimetric (CPOL) radar described in Fridlind et al. (2012).

The 23 January MCS event was the single most intense rainfall event observed during the TWP-ICE campaign. It was spatially large (significantly larger than the experimental domain) and eventually developed a cyclonic circulation. Mapes and Houze (1993) suggested that concentrated vorticity associated with mesoscale convection provides mean ascent, which is a positive feedback for monsoon evolution. As noted by Raymond and Jiang (1990), the regions of vorticity induced by mesoscale convective systems are most effective at inducing ascent when they interact with environmental vertical shear. The fraction of the experimental domain covered by the convective and stratiform regions in the simulation and observations are respectively shown in Figs. 8c and 8d. Despite the fact that the rainfall rate is a good match with retrievals, the simulation overestimated the average convective coverage. Also note that starting from around the peak of the event, nearly the whole domain was observed to be covered with

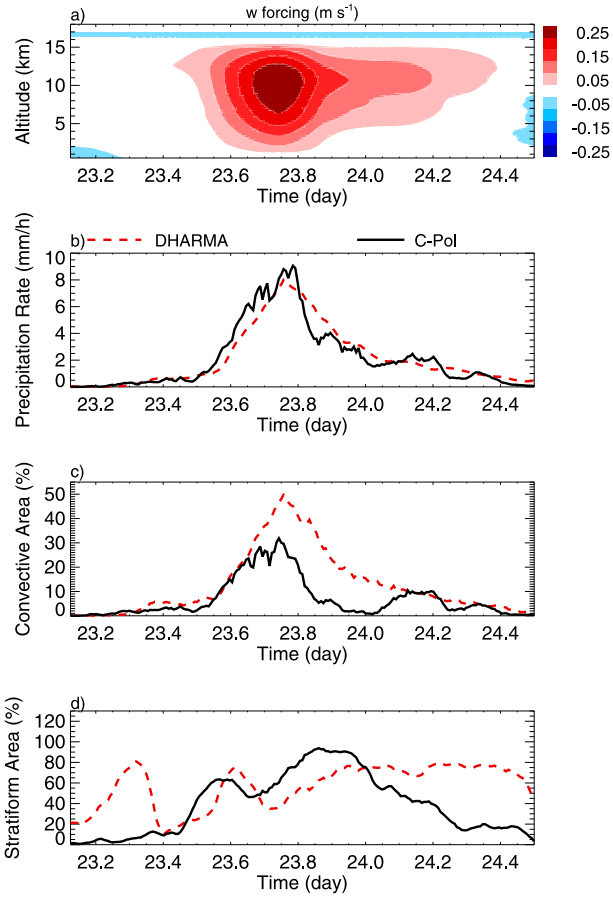

FIG. 8. (a) Time series of the large-scale vertical velocity forcing in the color contours. Time series of (b) precipitation rate, (c) stratiform area, and (d) convective area compared with CPOL radar observations below.

precipitating clouds. For the doubly periodic boundary conditions of that simulation, that meant the stratiform anvil that was gradually developed during the life cycle of the MCS could not be removed from the model domain and resulted in a substantial overestimation of stratiform region during the final phases of the simulation.

As noted in Mrowiec et al. (2012), the doubly periodic boundary conditions in the numerical setup require that the horizontal-mean resolved vertical velocity must be zero. Thus, the large-scale vertical velocity is not included in the model w. The way that we treat the vertical velocity field is important for model results interpretation. From the point of view of an observational framework, the large-scale vertical velocity should be included in the computations of mass fluxes. The temporal trend of large-scale vertical motion is smooth, but the vertical tendencies of moisture and heat that were used in simulations to avoid divergence of models from one another in the intercomparison study are not always as smooth. The latter may have introduced undesirable noise in simulations. It is likely preferable to apply vertical motion to model-predicted moisture and temperature fields in future studies, owing also to increased realism, despite potential impact on increasing simulation spread with advancing time. Figure 9a shows domain-averaged vertical velocity in the stratiform region for resolved motions, and in Fig. 9b, the large-scale vertical velocity field is included. The resolved motions are downward during the peak of the event, possibly in connection with melting and the boundary conditions forcing the subsidence to balance the convective updrafts. The total vertical wind between 7 km and the tropopause is, however, upward on average, a typical upper-tropospheric value of about 10 cm s^{-1}.

The convective mass transports with no large-scale vertical velocity and including the large-scale vertical velocity are shown in Figs. 10a and 10b, respectively. Analogous fields for the stratiform region are shown in Figs. 10c and 10d. The impact of the large scale is evidently much greater in the stratiform region than it is for the convective region, where the intensity of the vertical motions is much greater. In the stratiform region, the

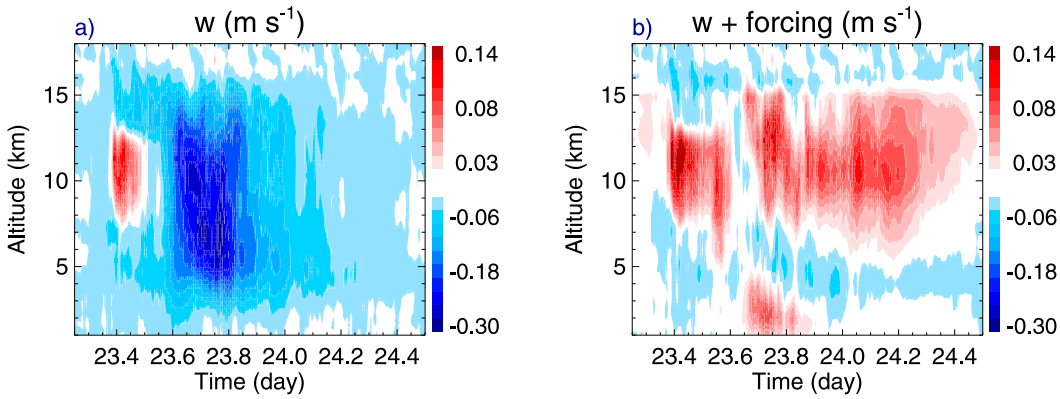

FIG. 9. Time series of the (a) averaged vertical velocity and (b) averaged vertical velocity including large-scale forcing in the stratiform region.

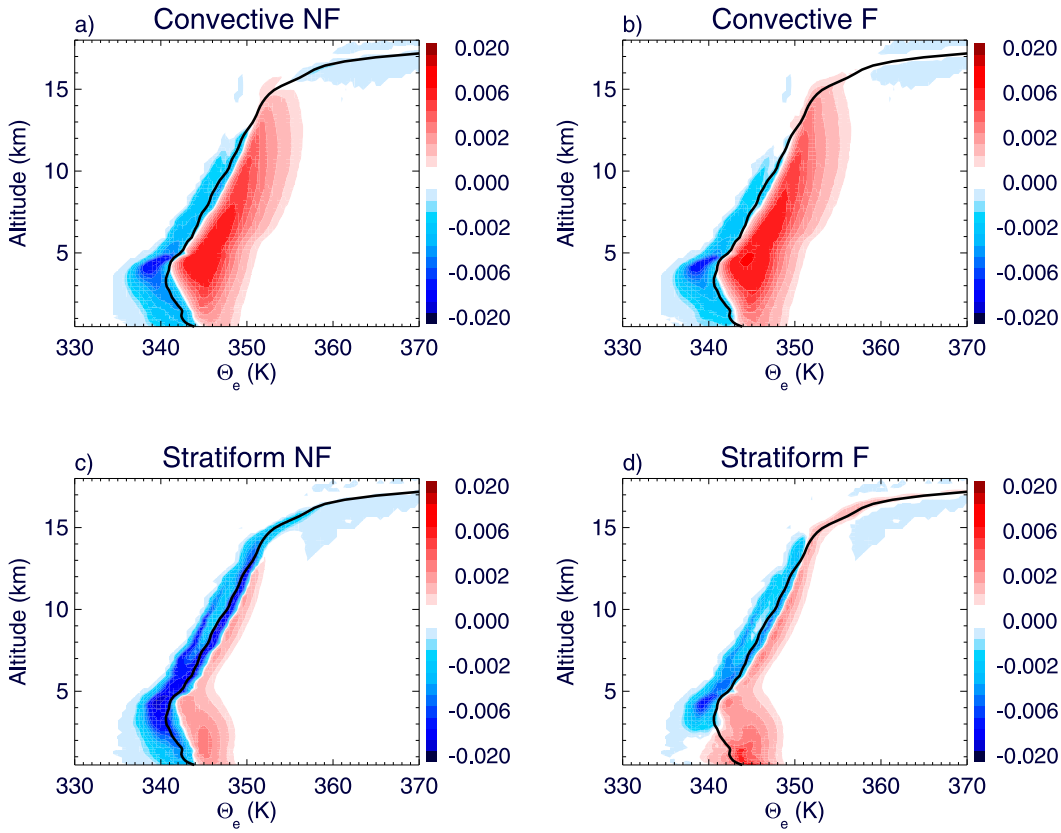

FIG. 10. Mass flux (b),(d) with and (a),(c) without large-scale forcing in (a),(b) convective and (c),(d) stratiform regions.

downward mass flux signal that extended from the tropopause down and peaked at the melting level is greatly weakened when the large-scale vertical winds are included. The downdrafts below the melting level that could reach the surface become rarer. The mesoscale downdrafts are comparable to the large-scale ascent. The mesoscale updraft, however, gets reinforced and extended upward.

The key point here is that, once the large-scale ascent is accounted for, ascent in the stratiform region (albeit relatively weak) is consistent with the "established" view of the mesoscale convective systems (Houze 1989). At the same time, the downdrafts get extremely weak (almost none of them reach the lowest levels) below the melting level when the large-scale ascent is included. The transition from downward to upward motion occurs at the melting level, not at 7 km, so that may be a bias in the simulation. This alters any interpretation of the resolved vertical velocity field associated with the stratiform regions.

6. Microphysics

In the presence of strong updrafts, the dominant growth mechanism for precipitation particles is the collection of the cloud water by raindrops and ice (coalescence and riming, respectively) (Houghton 1968). Strong updrafts extend the residence time of the larger particles within the cloud and thus result in larger hydrometeors. The microphysical growth processes of the convective precipitation (both liquid and frozen) formation are different from the stratiform precipitation areas. Vapor diffusion and aggregation increase particle size in both regions, but coalescence and riming are only important in convective regions (Houghton 1968; Houze 1997).

Graupel forms in strong convective updrafts. The number concentrations and mixing ratios for graupel in convective and stratiform regions are shown in Fig. 11. In the convective regions (specifically, convective cores), between 6 and 9 km and for the θ_e range between 355 and 360 K, the graupel mixing ratio increases gradually with height, but the number concentration is uniform, and updraft velocities (Fig. 5) are fairly constant as well. Above 10 km, the ambient temperature falls below −40°C, causing the homogeneous freezing of all remaining water droplets in the updrafts, thus increasing the number concentration and creating a maximum in the mixing ratio.

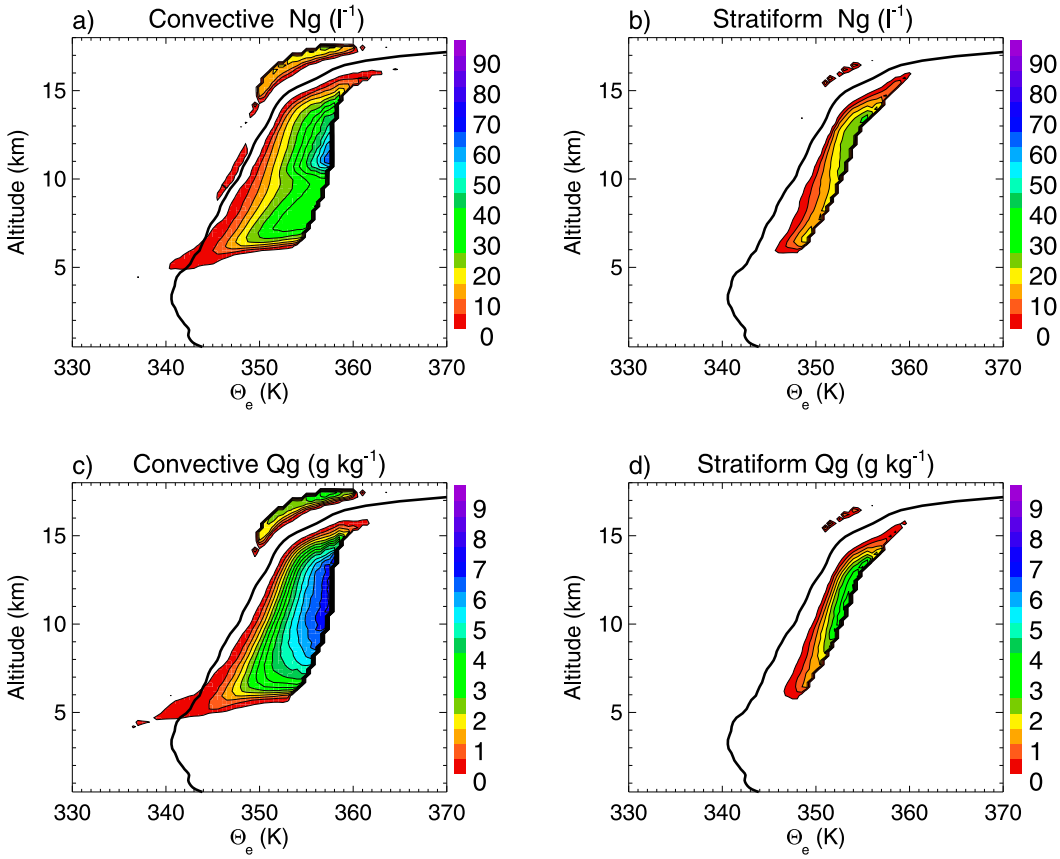

FIG. 11. (a),(b) Graupel number concentrations and (c),(d) mixing ratios in the (a),(c) convective and (b),(d) stratiform regions.

The partitioning and occurrence of snow are shown in Fig. 12. The structure of isentropic number concentration and mixing ratios are similar for snow and for graupel. In the convective region, the snow particles grow with height, between 6 and 10 km, at which point homogeneous freezing occurs, resulting in a maximum of the snow number concentration. Note that this maximum is located at a lower equivalent potential temperature and requires weaker vertical wind but spans a wide range of vertical velocities in contrast to graupel. The lowest level of graupel (or snow) occurrence is not at a constant altitude, because the melting level increases as updrafts become warmer with higher θ_e.

7. Conclusions

Here we implement the new technique developed in PM13 to studies of the convective overturning in a mesoscale convective system case study. We apply a conditional averaging of gridcell properties on equivalent potential temperature surfaces. In effect, the space- and time-dependent parameters are represented in terms of height, θ_e, and time. An equivalent potential temperature–based averaging preserves the separation between warm, moist updrafts and cooler, drier downdrafts that are fundamental aspects of moist convection. We focus on the isentropic mass flux and the isentropic streamfunction, tracing the average transport of thermodynamically similar air parcels within the convective subregions. In addition, the isentropic averaging filters out small gravity waves, which, as reversible oscillations, do not contribute to mass transport. It is shown that the isentropic analysis leads to systematically and considerably lower values for the mass transport relative to other techniques that include all vertical motions.

There is little resolved isentropic ascent in the stratiform region. Most of the ascent takes place in the convective region. However, when the imposed large-scale ascent is included in the analysis, the mesoscale ascent is stronger, but the mesoscale downdrafts get weaker and do not reach the lowest levels shown. Convective downdrafts are strongest at and just below the melting level, which shows the importance of melting for producing or strengthening downdrafts. Only when the large-scale forcing is included in the analysis does the stratiform-region vertical motion start to resemble the established

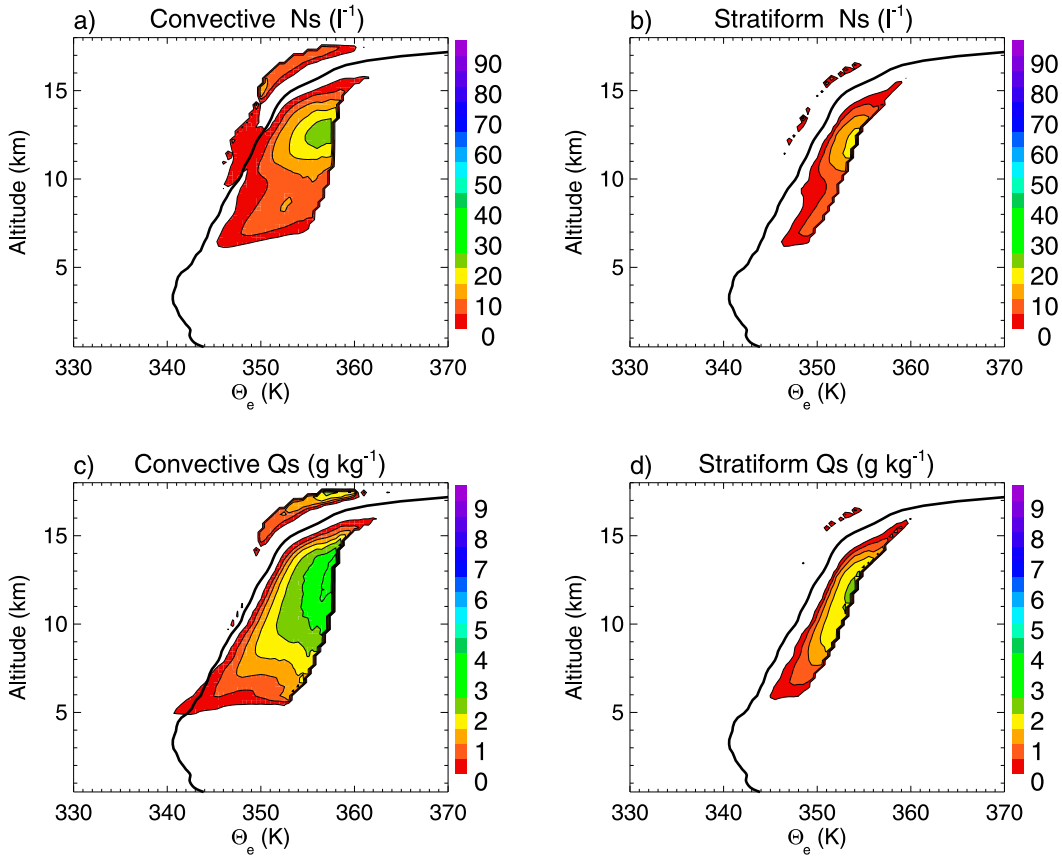

FIG. 12. (a),(b) Snow number concentrations and (c),(d) mixing ratios in the (a),(c) convective and (b),(d) stratiform regions.

schematic view of the MCS stratiform region. The simulations performed here were designed to be compared with single-column model simulations (cf. Davies et al. 2013; Petch et al. 2014), and extension of this analysis to limited-area model simulations would be desirable, especially with respect to stratiform-area properties [see Varble et al. (2014a,b) for comparison of these simulations with limited-area simulations].

Analysis of the streamfunction based on the isentropic mass flux identifies the convective overturning as a combination of ascent of high-energy air parcels and descent of air with much lower energy, shows the role of entrainment in reducing the equivalent potential temperature of the rising air parcels in the lower troposphere, and is consistent with a notable amount of overshooting in the tropopause region. The location of the isentropic streamfunction minimum in the MCS is different from the surface-driven RCE convection analyzed in PM13. To fully understand whether the location of the overturning maximum depends only on the type or strength of convection or to what extent the setup of the experiments is important, more studies need to be done. Future analysis could be repeated with a different isentropic-surface definition (one that takes into account the effects of ice freezing and melting). More cloud-resolving and LAM simulations could be set up, in which the sensitivity to the boundary layer and the forcing could be tested.

Other properties of rising and subsiding parcels, such as vertical velocity, buoyancy, and microphysical quantities can also be systematically recovered with the isentropic averaging approach. The strongest vertical velocities are very infrequent and associated with the deep, weakly diluted updrafts that exist at high values of equivalent potential temperatures. Large vertical velocities in the convective region are correlated with large graupel and snow mixing ratios. The number concentrations of the graupel and snow are doubled above 10 km, as raindrops freeze instantaneously to produce graupel and cloud drops freeze instantaneously to produce cloud ice, which then grow enough to become snow in about 2 km of subsequent ascent. The analysis shown here not only provides insight into the physical processes taking place in deep convection but also is informative regarding some aspects of microphysical parameterization. This analysis could be tested across different model setups (e.g., grid spacing affecting

entrainment, microphysics, and large-scale forcing) and validated with observations from field campaigns in future work.

The approach presented here is well adapted for analysis of simulated convection and applies to a variety of numerical model setups. This feature can be valuable for model intercomparisons and diagnostics of the convective transport in increasingly complex numerical models. The isentropic analysis is an efficient, complementary method for studying thermodynamic and microphysical properties of convective overturning. Direct computation of the isentropic streamfunction requires high-resolution (both spatial and temporal) data. It might be possible, however, to approximate it on a statistical basis using the statistical transformed Eulerian-mean circulation (Pauluis et al. 2011). Hence, the isentropic streamfunction could potentially be used as an intermediary diagnostic for comparisons between high-resolution cloud-resolving models and single-column models.

Acknowledgments. This research was supported by the DOE Office of Science, Office of Biological and Environmental Research, through Contract DE-PS02-09ER09-01 (Mrowiec) within the scope of the FASTER Project. Computational support was provided by the DOE National Energy Research Scientific Computing Center and the NASA Advanced Supercomputing Division. TWP-ICE data were obtained from the ARM program archive, sponsored by the DOE Office of Science, Office of Biological and Environmental Research, Environmental Science Division.

REFERENCES

Ackerman, A. S., O. B. Toon, D. E. Stevens, A. J. Heymsfield, V. Ramanathan, and E. J. Welton, 2000: Reduction of tropical cloudiness by soot. *Science,* **288,** 1042–1047, doi:10.1126/science.288.5468.1042.

Alexander, M. J., J. R. Holton, and D. R. Durran, 1995: The gravity wave response above deep convection in a squall line simulation. *J. Atmos. Sci.,* **52,** 2212–2226, doi:10.1175/1520-0469(1995)052<2212:TGWRAD>2.0.CO;2.

Biggerstaff, M. I., and R. A. Houze Jr., 1991: Kinematic and precipitation structure of the 10–11 June 1985 squall line. *Mon. Wea. Rev.,* **119,** 3034–3065, doi:10.1175/1520-0493(1991)119<3034:KAPSOT>2.0.CO;2.

——, and ——, 1993: Kinematics and microphysics of the transition zone of the 10–11 June 1985 squall line. *J. Atmos. Sci.,* **50,** 3091–3110, doi:10.1175/1520-0469(1993)050<3091:KAMOTT>2.0.CO;2.

Bretherton, C. S., and P. K. Smolarkiewicz, 1989: Gravity waves, compensating subsidence and detrainment around cumulus clouds. *J. Atmos. Sci.,* **46,** 740–759. doi:10.1175/1520-0469(1989)046<0740:GWCSAD>2.0.CO;2.

Davies, L., and Coauthors, 2013: A single-column model ensemble approach applied to the TWP-ICE experiment. *J. Geophys. Res. Atmos.,* **118,** 6544–6563, doi:10.1002/jgrd.50450.

Del Genio, A., and J. Wu, 2010: The role of entrainment in the diurnal cycle of continental convection. *J. Climate,* **23,** 2722–2738, doi:10.1175/2009JCLI3340.1.

Dunkerton, T. J., 1997: The role of gravity waves in the quasi-biennial oscillation. *J. Geophys. Res.,* **102,** 26 053–26 076, doi:10.1029/96JD02999.

Emanuel, K. A., 1994: *Atmospheric Convection.* Oxford University Press, 580 pp.

Fridlind, A. M., A. S. Ackerman, J. C. Petch, P. R. Field, A. Hill, G. McFarquhar, S. Xie, and M. Zhang, 2010: ARM/GCSS/SPARC TWP-ICE CRM intercomparison study. NASA Tech. Rep. NASA/TM–2010–215 858, 26 pp.

——, and Coauthors, 2012: A comparison of TWP-ICE observational data with cloud-resolving model results. *J. Geophys. Res.,* **117,** D05204, doi:10.1029/2011JD016595.

Grim, J. A., G. M. McFarquhar, R. M. Rauber, A. M. Smith, and B. F. Jewett, 2009: Microphysical and thermodynamic structure and evolution of the trailing stratiform regions of mesoscale convective systems during BAMEX. Part II: Column model simulations. *Mon. Wea. Rev.,* **137,** 1186–1205, doi:10.1175/2008MWR2505.1.

Houghton, H. G., 1968: On precipitation mechanisms and their artificial modification. *J. Appl. Meteor.,* **7,** 851–859, doi:10.1175/1520-0450(1968)007<0851:OPMATA>2.0.CO;2.

Houze, R. A., Jr., 1989: Observed structure of mesoscale convective systems and implications for large-scale heating. *Quart. J. Roy. Meteor. Soc.,* **115,** 425–461, doi:10.1002/qj.49711548702.

——, 1997: Stratiform precipitation in regions of convection: A meteorological paradox? *Bull. Amer. Meteor. Soc.,* **78,** 2179–2196, doi:10.1175/1520-0477(1997)078<2179:SPIROC>2.0.CO;2.

——, 2004: Mesoscale convective systems. *Rev. Geophys.,* **42,** RG4003, doi:10.1029/2004RG000150.

Khain, A. P., V. Phillips, N. Benmoshe, and A. Pokrovsky, 2012: The role of small soluble aerosols in the microphysics of deep maritime clouds. *J. Atmos. Sci.,* **69,** 2787–2807, doi:10.1175/2011JAS3649.1.

Khairoutdinov, M. F., and D. A. Randall, 2003: Cloud resolving modeling of the ARM summer 1997 IOP: Model formulation, results, uncertainties, and sensitivities. *J. Atmos. Sci.,* **60,** 607–625, doi:10.1175/1520-0469(2003)060<0607:CRMOTA>2.0.CO;2.

Lane, T. P., M. J. Reeder, and T. L. Clark, 2001: Numerical modeling of gravity wave generation by deep tropical convection. *J. Atmos. Sci.,* **58,** 1249–1274, doi:10.1175/1520-0469(2001)058<1249:NMOGWG>2.0.CO;2.

Lang, S., W.-K. Tao, J. Simpson, and B. Ferrier, 2003: Modeling of convective – stratiform precipitation processes: Sensitivity to partitioning methods. *J. Appl. Meteor.,* **42,** 505–527, doi:10.1175/1520-0450(2003)042<0505:MOCSPP>2.0.CO;2.

Lin, Y.-L., R. Deal, and M. S. Kulie, 1998: Mechanisms of cell regeneration, development, and propagation within a two-dimensional multicell storm. *J. Atmos. Sci.,* **55,** 1867–1886, doi:10.1175/1520-0469(1998)055<1867:MOCRDA>2.0.CO;2.

Mapes, B. E., 1993: Gregarious tropical convection. *J. Atmos. Sci.,* **50,** 2026–2037. doi:10.1175/1520-0469(1993)050<2026:GTC>2.0.CO;2.

——, and R. A. Houze, Jr., 1993: An integrated view of the 1987 Australian monsoon and its mesoscale convective systems. II: Vertical structure. *Quart. J. Roy. Meteor. Soc.,* **119,** 733–754, doi:10.1002/qj.49711951207.

May, P. T., J. H. Mather, G. Vaughan, K. N. Bower, C. Jakob, G. M. McFarquhar, and G. G. Mace, 2008: The Tropical Warm Pool

International Cloud Experiment. *Bull. Amer. Meteor. Soc.,* **89,** 629–645, doi:10.1175/BAMS-89-5-629.

McFarlane, S. A., K. F. Evans, and A. S. Ackerman, 2002: A Bayesian algorithm for the retrieval of liquid water cloud properties from microwave radiometer and millimeter radar data. *J. Geophys. Res.,* **107,** doi:10.1029/2001JD001011.

Morrison, H., G. Thompson, and V. Tatarskii, 2009: Impact of cloud microphysics on the development of trailing stratiform precipitation in a simulated squall line: Comparison of one- and two-moment schemes. *Mon. Wea. Rev.,* **137,** 991–1007, doi:10.1175/2008MWR2556.1.

Mrowiec, A. A., C. Rio, A. M. Fridlind, A. S. Ackerman, A. D. Del Genio, O. Pauluis, A. Varble, and J. Fan, 2012: Analysis of cloud-resolving simulations of a tropical mesoscale convective system observed during TWP-ICE: Vertical fluxes and draft properties in convective and stratiform regions. *J. Geophys. Res.,* **117,** D19201, doi:10.1029/2012JD017759.

Ogura, Y., and N. A. Phillips, 1962: Scale analysis of deep and shallow convection in the atmosphere. *J. Atmos. Sci.,* **19,** 173–179, doi:10.1175/1520-0469(1962)019<0173:SAODAS>2.0.CO;2.

Pauluis, O. M., and A. A. Mrowiec, 2013: Isentropic analysis of convective motions. *J. Atmos. Sci.,* **70,** 3673–3688, doi:10.1175/JAS-D-12-0205.1.

——, A. Czaja, and R. Korty, 2008: The global atmospheric circulation on moist isentropes. *Science,* **321,** 1075–1078, doi:10.1126/science.1159649.

——, ——, and ——, 2010: The global atmospheric circulation in moist isentropic coordinates. *J. Climate,* **23,** 3077–3093, doi:10.1175/2009JCLI2789.1.

——, T. Shaw, and F. Laliberté, 2011: A statistical generalization of the transformed Eulerian-mean circulation for an arbitrary vertical coordinate system. *J. Atmos. Sci.,* **68,** 1766–1783, doi:10.1175/2011JAS3711.1.

Petch, J., A. Hill, L. Davies, A. Fridlind, C. Jakob, Y. Lin, S. Xie, and P. Zhu, 2014: Evaluation of intercomparisons of four different types of model simulating TWP-ICE. *Quart. J. Roy. Meteor. Soc.,* **140,** 826–837, doi:10.1002/qj.2192.

Piani, C., D. Durran, M. Alexander, and J. Holton, 2000: A numerical study of three-dimensional gravity waves triggered by deep tropical convection and their role in the dynamics of the QBO. *J. Atmos. Sci.,* **57,** 3689–3702, doi:10.1175/1520-0469(2000)057<3689:ANSOTD>2.0.CO;2.

Raymond, D. J., and H. Jiang, 1990: A theory for long-lived mesoscale convective systems. *J. Atmos. Sci.,* **47,** 3067–3077, doi:10.1175/1520-0469(1990)047<3067:ATFLLM>2.0.CO;2.

Rossby, C.-G., 1937: Isentropic analysis. *Bull. Amer. Meteor. Soc.,* **18,** 201–209.

Shaw, S. N., 1930: *The Physical Processes of Weather.* Vol. 3, *Manual of Meteorology,* Cambridge University Press, 474 pp.

Steiner, M., R. A. Houze Jr., and S. E. Yuter, 1995: Climatological characterization of three-dimensional storm structure from operational radar and rain gauge data. *J. Appl. Meteor.,* **34,** 1978–2007, doi:10.1175/1520-0450(1995)034<1978:CCOTDS>2.0.CO;2.

Stevens, D. E., and S. Bretherton, 1996: A forward-in-time advection scheme and adaptive multilevel flow solver for nearly incompressible atmospheric flow. *J. Comput. Phys.,* **129,** 284–295, doi:10.1006/jcph.1996.0250.

——, A. S. Ackerman, and C. S. Bretherton, 2002: Effects of domain size and numerical resolution on the simulation of shallow cumulus convection. *J. Atmos. Sci.,* **59,** 3285–3301, doi:10.1175/1520-0469(2002)059<3285:EODSAN>2.0.CO;2.

Toon, O. B., C. P. McKay, T. P. Ackerman, and K. Santhanam, 1989: Rapid calculation of radiative heating rates and photodissociation rates in inhomogeneous multiple scattering atmospheres. *J. Geophys. Res.,* **94,** 16 287–16 301, doi:10.1029/JD094iD13p16287.

Townsend, R. D., and D. R. Johnson, 1985: A diagnostic study of the isentropic zonally averaged mass circulation during the First GARP Global Experiment. *J. Atmos. Sci.,* **42,** 1565–1579, doi:10.1175/1520-0469(1985)042<1565:ADSOTI>2.0.CO;2.

Varble, A., and Coauthors, 2011: Evaluation of cloud-resolving model intercomparison simulations using TWP-ICE observations: Precipitation and cloud structure. *J. Geophys. Res.,* **116,** D12206, doi:10.1029/2010JD015180.

——, and Coauthors, 2014a: Evaluation of cloud-resolving and limited area model intercomparison simulations using TWP-ICE observations: 1. Deep convective updraft properties. *J. Geophys. Res. Atmos.,* **119**, 13 891–13 918, doi:10.1002/2013JD021371.

——, and Coauthors, 2014b: Evaluation of cloud-resolving and limited area model intercomparison simulations using TWP-ICE observations: 2. Precipitation microphysics. *J. Geophys. Res. Atmos.,* **119**, 13 919–13 945, doi:10.1002/2013JD021372.

Xie, S., T. Hume, C. Jakob, S. A. Klein, R. B. McCoy, and M. Zhang, 2010: Observed large-scale structures and diabatic heating and drying profiles during TWP-ICE. *J. Climate,* **23,** 57–79, doi:10.1175/2009JCLI3071.1.

Xu, K.-M., and K. A. Emanuel, 1989: Is the tropical atmosphere conditionally unstable? *Mon. Wea. Rev.,* **117,** 1471–1479, doi:10.1175/1520-0493(1989)117<1471:ITTACU>2.0.CO;2.

Zhang, M. H., and J. L. Lin, 1997: Constrained variational analysis of sounding data based on column-integrated budgets of mass, heat, moisture, and momentum: Approach and application to ARM measurements. *J. Atmos. Sci.,* **54,** 1503–1524, doi:10.1175/1520-0469(1997)054<1503:CVAOSD>2.0.CO;2.

Zhu, P., and Coauthors, 2012: A limited area model (LAM) intercomparison study of a TWP-ICE active monsoon mesoscale convective event. *J. Geophys. Res.,* **117,** D11208, doi:10.1029/2011JD016447.